The 2L1S/1L2S Degeneracy for Two Microlensing Planet Candidates Discovered by the KMTNet Survey in 2017

I.-G. Shin[1,2] , J. C. Yee[2] , A. Gould[1,3,4], M. T. Penny[3] , I. A. Bond[5],
and
M. D. Albrow[6] , S.-J. Chung[1,7] , C. Han[8] , K.-H. Hwang[1] , Y. K. Jung[1] , Y.-H. Ryu[1] , Y. Shvartzvald[9] , S.-M. Cha[1,10],
D.-J. Kim[1], H.-W. Kim[1,7] , S.-L. Kim[1,7], C.-U. Lee[1,7], D.-J. Lee[1], Y. Lee[1,10], B.-G. Park[1,7], R. W. Pogge[3]
(KMTNet Collaboration),
F. Abe[11], R. Barry[12], D. P. Bennett[12], A. Bhattacharya[12,13], M. Donachie[14], H. Fujii[11], A. Fukui[15] , Y. Hirao[16], Y. Itow[11] ,
Y. Kamei[11], Iona Kondo[16] , N. Koshimoto[16], M. C. A. Li[14], Y. Matsubara[11], S. Miyazaki[16] , Y. Muraki[11], M. Nagakane[16],
C. Ranc[12,24] , N. J. Rattenbury[14] , Harmon Suematsu[16], D. J. Sullivan[17], T. Sumi[16], Daisuke Suzuki[18] , P. J. Tristram[19],
T. Yamakawa[11], A. Yonehara[20]
(MOA Collaboration),
and
P. Fouqué[21,22], and W. Zang[23]
(CFHT-K2C9 Microlensing Collaboration)

[1] Korea Astronomy and Space Science Institute, 776 Daedeokdae-ro, Yuseong-Gu, Daejeon 34055, Republic of Korea
[2] Harvard-Smithsonian Center for Astrophysics, 60 Garden St., Cambridge, MA 02138, USA
[3] Department of Astronomy, Ohio State University, 140 W. 18th Ave., Columbus, OH 43210, USA
[4] Max-Planck-Institute for Astronomy, Königstuhl 17, D-69117 Heidelberg, Germany
[5] Institute of Natural and Mathematical Sciences, Massey University, Auckland 0745, New Zealand
[6] University of Canterbury, Department of Physics and Astronomy, Private Bag 4800, Christchurch 8020, New Zealand
[7] Korea University of Science and Technology, UST, 217 Gajeong-ro Yuseong-gu, Daejeon 34113, Republic of Korea
[8] Department of Physics, Chungbuk National University, Cheongju 28644, Republic of Korea
[9] IPAC, Mail Code 100-22, Caltech, 1200 E. California Blvd., Pasadena, CA 91125, USA
[10] School of Space Research, Kyung Hee University, Giheung-gu, Yongin, Gyeonggi-do, 17104, Republic of Korea
[11] Institute for Space-Earth Environmental Research, Nagoya University, Nagoya 464-8601, Japan
[12] Code 667, NASA Goddard Space Flight Center, Greenbelt, MD, USA
[13] Department of Astronomy, University of Maryland, College Park, MD, USA
[14] Department of Physics, University of Auckland, Private Bag 92019, Auckland, New Zealand
[15] Okayama Astrophysical Observatory, National Astronomical Observatory of Japan, 3037-5 Honjo, Kamogata, Asakuchi, Okayama 719-0232, Japan
[16] Department of Earth and Space Science, Graduate School of Science, Osaka University, Toyonaka, Osaka 560-0043, Japan
[17] School of Chemical and Physical Sciences, Victoria University, Wellington, New Zealand
[18] Institute of Space and Astronautical Science, Japan Aerospace Exploration Agency, Kanagawa 252-5210, Japan
[19] University of Canterbury Mount John Observatory, P.O. Box 56, Lake Tekapo 8770, New Zealand
[20] Department of Physics, Faculty of Science, Kyoto Sangyo University, 603-8555 Kyoto, Japan
[21] CFHT Corporation, 65-1238 Mamalahoa Hwy., Kamuela, Hawaii 96743, USA
[22] Université de Toulouse, UPS-OMP, IRAP, Toulouse, France
[23] Physics Department and Tsinghua Centre for Astrophysics, Tsinghua University, Beijing 100084, People's Republic of China

Abstract

We report two microlensing planet candidates discovered by the Korea Microlensing Telescope Network (KMTNet) survey in 2017. However, both events have the 2L1S/1L2S degeneracy, which is an obstacle to claiming the discovery of the planets with certainty unless the degeneracy can be resolved. For KMT-2017-BLG-0962, the degeneracy cannot be resolved. If the 2L1S solution is correct, KMT-2017-BLG-0962 might be produced by a super Jupiter-mass planet orbiting a mid-M-dwarf host star. For KMT-2017-BLG-1119, the light-curve modeling favors the 2L1S solution but higher-resolution observations of the baseline object tend to support the 1L2S interpretation rather than the planetary interpretation. This degeneracy might be resolved by a future measurement of the lens-source relative proper motion. This study shows that the problem of resolving 2L1S/1L2S degeneracy exists over a much wider range of conditions than those considered by the theoretical study of Gaudi (1998).

Key words: planets and satellites: detection – gravitational lensing: micro

1. Introduction

The basic requirements for the statistical studies of planets are detections of planets and the determination of planet properties. However, discoveries and characterizations of microlensing planets depend on the interpretation of anomalies in the observed light curves. Even when these anomalies can be described by a planetary model, alternative interpretations may exist that also provide sufficient descriptions for the putative planetary anomalies. In other words, degenerate solutions of the light curves can be obstacles to prevent either secure discoveries of planets or the unique determination of their properties.

---

[24] NASA Postdoctoral Program Fellow.

For example, the degeneracy between two interpretations of the binary-lens and single source (2L1S) and the single-lens and binary source (1L2S) can be a severe obstacle. If this 2L1S/1L2S degeneracy exists, we cannot claim a secure discovery of the planet unless the degeneracy is resolved. Gaudi (1998) first pointed out this 2L1S/1L2S degeneracy by showing that a certain class of the 1L2S model can resemble a planetary anomaly in the lensing light curve. In particular, that work focused on planetary events that exhibit small, short-duration positive deviations from a single-lens, single-source (1L1S) light curve. To produce a similar anomaly in the light curve using a 1L2S model, the brightness of the companion should be much fainter than the primary (the flux ratio of the secondary and primary, $\epsilon \equiv F_2/F_1$, should be from $\epsilon \sim 10^{-2}$ to $\sim 10^{-4}$). In addition, the companion should pass very close (in projection) to the lens (this impact factor for the secondary, $u_{0,S2}$, depends on the maximum amplitude, $\delta_{\max}$, of the planet-like anomaly with the flux ratio: $u_{0,S2} \lesssim \epsilon/\delta_{\max}$).

Indeed, there are discoveries of microlensing planet candidates, which could be interpreted by both 2L1S and 1L2S models. Beaulieu et al. (2006) found a clear planetary deviation (i.e., a small, short-duration positive deviation) in a microlensing event, OGLE-2005-BLG-390. They also found the 2L1S/1L2S degeneracy that plausibly described the anomaly. However, the 1L2S interpretation was rejected by the detailed light-curve analysis. Thus, they could claim the secure discovery of a planet, whose mass they estimated to be 5.5 $M_\oplus$. Hwang et al. (2013) also showed a microlensing event that had the 2L1S/1L2S degeneracy. The light curve of this work exhibits a planet-like anomaly (i.e., the strong positive deviation) that can be explained by either the 2L1S (including a planet) or 1L2S interpretation. They successfully resolved this degeneracy using multiband observations, revealing that the event was produced by two sources, rather than a planetary system. In addition, Dominik et al. (2019) recently presented a long timescale ($t_E \sim 300$ days) microlensing event, which can be explained either 2L1S or 1L2S interpretation. Their 2L1S model indicates that the lens system might be a planet with the mass of $\sim 45\,M_\oplus$ orbiting an M-dwarf host star ($\sim 0.35\,M_\odot$). However, they also find a competitive 1L2S model that indicates that the lens might be a brown dwarf ($0.046\,M_\odot$). The light-curve data cannot resolve this degeneracy, but they suggest that future observations may be able to resolve this severe degeneracy.

However, in practice, we have found that the 2L1S/1L2S degeneracy can be extended to cases beyond the extreme flux case considered by Gaudi (1998), e.g., Jung et al. (2017b), Dominik et al. (2019), and events in this work. In Jung et al. (2017b), the light curve of the event showed a broad asymmetry with small additional deviations in the wing. This anomaly can be adequately described by both the 2L1S (i.e., a planetary lens system) and the 1L2S interpretations. This event was produced by approximately equally luminous binary sources in contrast to the case of Gaudi (1998). They resolved this degeneracy using detailed modeling of the densely covered light curve. In Dominik et al. (2019), they showed that the planet-like anomaly in the 2L1S case could be produced when the source passes close to the central caustic, i.e., a high-magnification, event. This anomaly is different from Gaudi's case, which is produced when the source approaches one planetary caustic. They noted that the 1L2S model with a small

flux ratio of binary sources can produce this planet-like anomaly in contrast to Gaudi's case.

In addition, microlensing events show that more complex anomalies have been found. These events can be described by more complicated multiple-lens and multiple-source interpretations. For example, Jung et al. (2017a) showed a degeneracy caused by 3L1S and 2L2S interpretations. Moreover, Hwang et al. (2018) showed an extreme case (i.e., an exo-moon candidate) of a three-fold degeneracy with 3L1S, 2L2S, and 1L3S interpretations. In particular, the degeneracy becomes severe when the observations do not optimally cover the anomalies in the light curves.

Here we analyze two microlensing events, KMT-2017-BLG-0962 and KMT-2017-BLG-1119, which were discovered in 2017 by the Korea Microlensing Telescope Network (KMTNet; Kim et al. 2016). We reveal that these events are planet candidates by analyzing the light curves using the 2L1S interpretation. For KMT-2017-BLG-0962, the mass ratio ($q = M_{\mathrm{planet}}/M_{\mathrm{host}}$) is ~ 0.01, which indicates that the companion in the lens system might be a Jupiter-class planet under the assumption of an M-dwarf host star. For KMT-2017-BLG-1119, the mass ratio is ~ 0.01, which also indicates that the lens component might be a planet. Moreover, the Einstein timescale (t_E) of this event is very short, i.e., $t_E \sim 2.9$ days. This short timescale implies that the event can be produced by a very low-mass planetary lens system.[25] However, both light curves can also be well described using the 1L2S interpretation.

We present observations of these planet candidates in Section 2. In Section 3, we present analyses of the light curves and the degeneracies. Then, we discuss the possibilities of resolving the degeneracies in Section 4. In Section 5, we present the possible properties of planet candidates determined using the Bayesian analyses. Lastly, in Section 6, we present our conclusion with the difference between a Gaudi (1998)-type degeneracy and this work. Additionally, we provide details of the 1L2S interpretations for the modeling in Appendix A. We also present tests for higher-order effects of the models to discuss non-detections of them in Appendix B.

2. KMTNet Observations

KMTNet is a second-generation microlensing survey consisting of a telescope network composed of three identical 1.6 m telescopes located at three sites in the southern hemisphere: the Cerro Tololo Inter-American Observatory in Chile (KMTC), the South African Astronomical Observatory in South Africa (KMTS), and the Siding Spring Observatory in Australia (KMTA). These well-separated time zones can provide near-continuous observations, weather permitting. In addition, the cameras of the KMTNet survey have a wide field of view (FOV: 4 deg^2). These wide FOVs yield high-cadence observations that are optimized to capture planetary anomalies caused by various types of planets. Thus, in general, the KMTNet survey (i.e., a second-generation microlensing survey) is less dependent on follow-up observations.

KMTNet discovered the two planet candidates presented in this work. The events were found by the KMTNet Event Finder

---

[25] The Einstein timescale is a crossing time that the source transverses the Einstein ring radius (θ_E), i.e., $t_E \propto \theta_E$. The size of θ_E is directly related to the mass of the lens system (M), i.e., $\theta_E \propto \sqrt{M/D_{\mathrm{rel}}}$ where $D_{\mathrm{rel}} \equiv (D_L^{-1} - D_S^{-1})^{-1}$. D_L and D_S are distances to the lens and source, respectively. Thus, $t_E \propto \sqrt{M}$, which is of the order of a month for typical microlensing events.

algorithm (Kim et al. 2018), which was run after the end of the 2017 microlensing season. No real-time alert was issued for these events, either by KMTNet or other microlensing groups. Hence, no useful real-time photometric follow-up observations were taken.[26]

However, we found that KMT-2017-BLG-1119 was located within the footprint of another survey. The Microlensing Observations in Astrophysics (MOA; Sumi et al. 2003) survey observed this event using the 1.8 m MOA-II telescope located at the Mount John Observatory in New Zealand, with the customized filter called the MOA-Red filter (wide $R + I$ filter). Because the MOA survey did not alert this event during the 2017 season, we separately requested the MOA data of the event. The data were reduced using their pipeline, which employed the difference image analysis (DIA) photometry (Bond et al. 2001). In contrast, KMT-2017-BLG-0962 is not located in the MOA observation fields.

2.1. KMT-2017-BLG-0962

KMT-2017-BLG-0962 occurred on source(s) located at $(\alpha, \delta)_{J2000} = (17^h46^m48^s54, -26°10'48''07)$ corresponding to the Galactic coordinates $(l, b) = (2°49,1°21)$. This event is located in the KMT-field BLG18 (see Figure 12 of Kim et al. 2018), which has the nominal observational cadence of 1 hr^{-1}. During the event, the cadence was 1 hr^{-1} at KMTC. For the other observations, the cadence was 0.75 hr^{-1}. In Figure 1, we present KMTNet observations of this event with a 1L1S model curve as a reference to clearly show the anomaly in the light curve. Clear perturbations exist around the peak of the event, HJD$'$(=HJD − 2450,000) ~ 7871.5.

2.2. KMT-2017-BLG-1119

KMT-2017-BLG-1119 occurred on source(s) located at $(\alpha, \delta)_{J2000} = (17^h52^m10^s63, -33°01'05''30)$ corresponding to the Galactic coordinates $(l, b) = (- 2°78, - 3°30)$. This event is located in the KMT-field, BLG22, which also has the nominal cadence 1 hr^{-1}. During the event, this was an actual cadence for KMTC observations. For KMTS and KMTA observations, the cadence was switched from 1 hr^{-1} to 0.75 hr^{-1} at HJD$'$ ~ 7971.25, i.e., just after the event peaked. In Figure 2, we present the KMTNet and MOA observations of this event. The observations show clear deviations (from HJD$'$ ~7967.5 to ~7969.0) from the 1L1S model.

3. Interpretations of the Light Curves

Because both events show clear anomalies in the observed light curves, we analyze the light curves using both 2L1S and 1L2S interpretations. For each interpretation, we build model light curves using an appropriate parameterization. Then, we minimize the χ^2 difference between the model and observations by using a Markov Chain Monte Carlo (MCMC) algorithm (Dunkley et al. 2005).

During the modeling process, the uncertainties of observations are rescaled using the equation $e_{new} = \kappa_{obs} e_{old}$, where the e_{new} and e_{old} are rescaled and original uncertainties in magnitudes, respectively.[27] The coefficient κ_{obs}, an error rescaling factor for each data set, is defined based on the best-fit model with the lowest χ^2 value. By making sure each data point contributes on average $\Delta\chi^2 \sim 1$, we can quantitatively compare the degenerate models. For KMT-2017-BLG-0962 and KMT-2017-BLG-1119, the sets of error rescaling factors are $(\kappa_{KMTC}, \kappa_{KMTS}, \kappa_{KMTA}) = (1.244, 1.239, 1.392)$ and $(\kappa_{KMTC}, \kappa_{KMTS}, \kappa_{KMTA}, \kappa_{MOA}) = (1.2208, 1.1209, 1.2017, 0.8930)$, respectively.

### 3.1. Parameterization of the 2L1S Interpretation

To build a standard 2L1S model light curve, seven basic parameters are required to describe the caustic form and the source trajectory. Two parameters (s and q) determine the caustic form. The value s represents the projected separation between the lenses in units of the angular Einstein ring radius (θ_E). Conventionally, cases of $s < 1$ and $s > 1$ are referred to "close" and "wide," respectively. The mass ratio of the lenses is defined as $q = M_2/M_1$ where M_1 and M_2 are masses of first and second bodies, respectively. These close and wide cases can yield a close/wide degeneracy caused by similarities in the magnification pattern, which are induced by an intrinsic symmetry in the lens equation (Griest & Safizadeh 1998; Dominik 1999).

Four parameters (t_0, u_0, t_E, and α) describe the source trajectory: t_0 is the time when the source most closely approaches to the reference position of the lens system (this reference position is the photocenter (Kim et al. 2009) defined as $s[1-(1+q)^{-1}]$ and $s^{-1}q/(1 + q)$ for the close ($s < 1$) and wide ($s > 1$) cases, respectively), u_0 is the separation at the time of t_0, t_E is the Einstein timescale defined as the time for the source to cross the Einstein ring radius of the event, and α is the angle of the source trajectory with respect to the binary axis of the lens system. The geometry of a microlensing event produced by 2L1S is built using these six parameters, which determine the magnification as a function of time, i.e., the microlensing light curve. The finite angular size of the source moderates the magnification. To account for the finite source effect, the final parameter, ρ_*, is required, which is defined as the angular source radius (θ_*) scaled by θ_E. In addition, we introduce two additional parameters, $F_{S,obs}$ (source flux) and $F_{B,obs}$ (blending flux), for each data set, which are used to scale the model to the data. These parameters are determined based on the model using the least-square fitting method.

3.2. Parameterization of the 1L2S Interpretation

A standard 1L2S model light curve is built using a superposition of two 1L1S light curves induced by each source. The trajectory of each source yields the individual

---

[26] KMT-2017-BLG-1119 was, in fact, serendipitously observed by the *Spitzer* satellite because it lies within the FOV of the InfraRed Array Camera (IRAC) of another event (OGLE-2017-BLG-0019) that was chosen for observations (see Yee et al. 2015). Unfortunately, these observations ended (due to Sun-angle restrictions) on JD-2450,000.0 ~ 7967.0, just two days before the peak of this very short event. In principle, if the lens were traveling approximately east, the source could nevertheless have been significantly magnified. However, we checked the images and found that the *Spitzer* light curve of KMT-2017-BLG-1119 is essentially flat. Thus, no meaningful constraints can be placed on this system from the *Spitzer* data.

[27] In general, the error rescaling is used a quadrature formalism: $e_{new} = \kappa\sqrt{e_{old}^2 + e_{min}^2}$, where κ and e_{min} are error rescaling factors. However, we find that the e_{min} factors should be zero for observations of both events. Thus, we only present the κ factor without the meaningless zero terms. In principle, the κ factor has an uncertainty of $(2N)^{-1/2}$. Neglecting this factor can affect the interpretation of the $\Delta\chi^2$ difference between two models. Specifically, it leads to an uncertainty in the $\Delta\chi^2$ of $\sqrt{(2/N)}$. Hence, $\sigma(\Delta\chi^2)/\Delta\chi^2 = \sqrt{(2/N)} \rightarrow 3.7\%$ for $N \sim 1500$, so that, for example, $\Delta\chi^2 = 10$ would formally be written as $\Delta\chi^2 = 10 \pm 0.37$ (for three observatories). This uncertainty in $\Delta\chi^2$ has no practical impact in the present case, so we suppress it in all expressions.
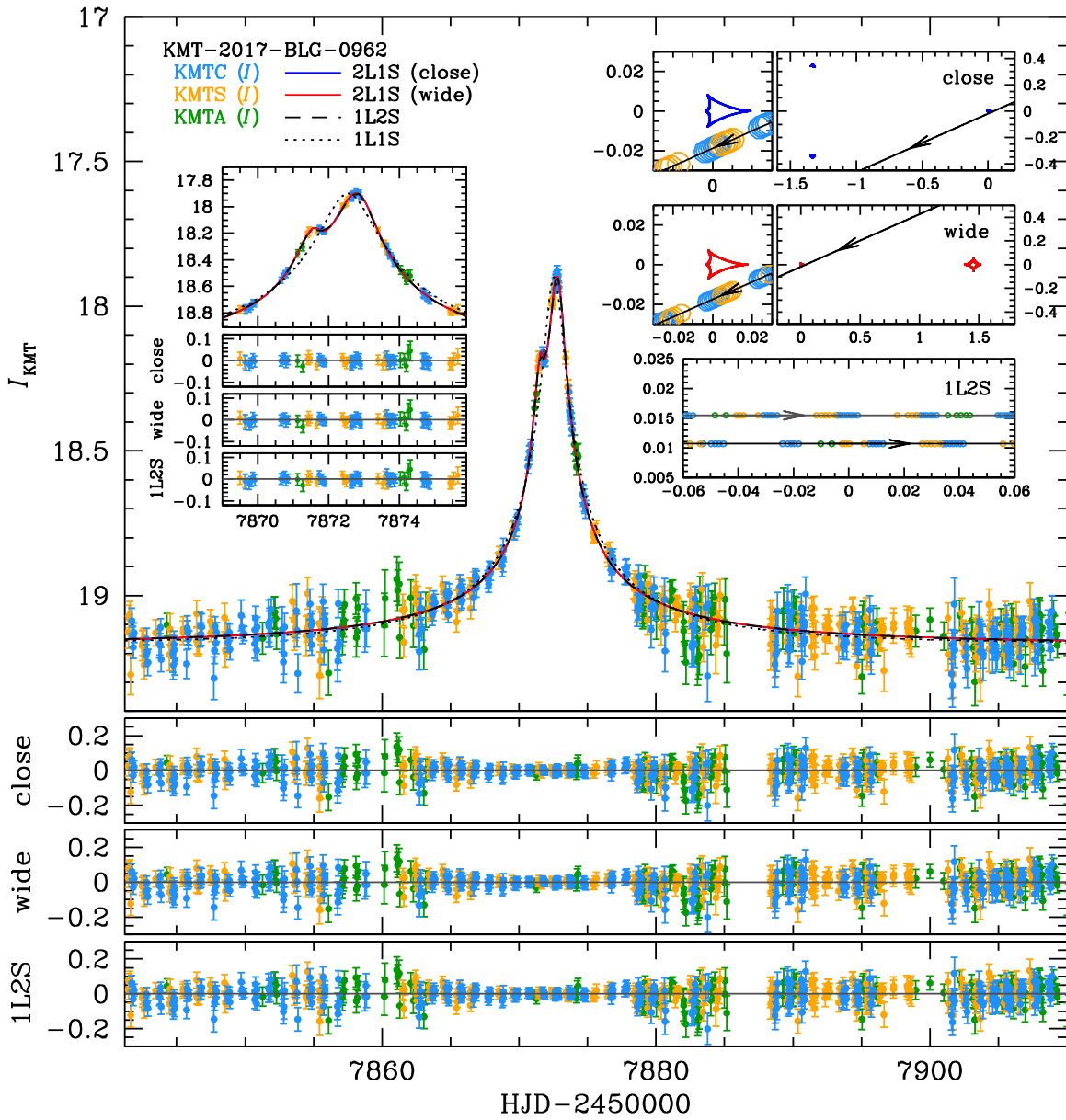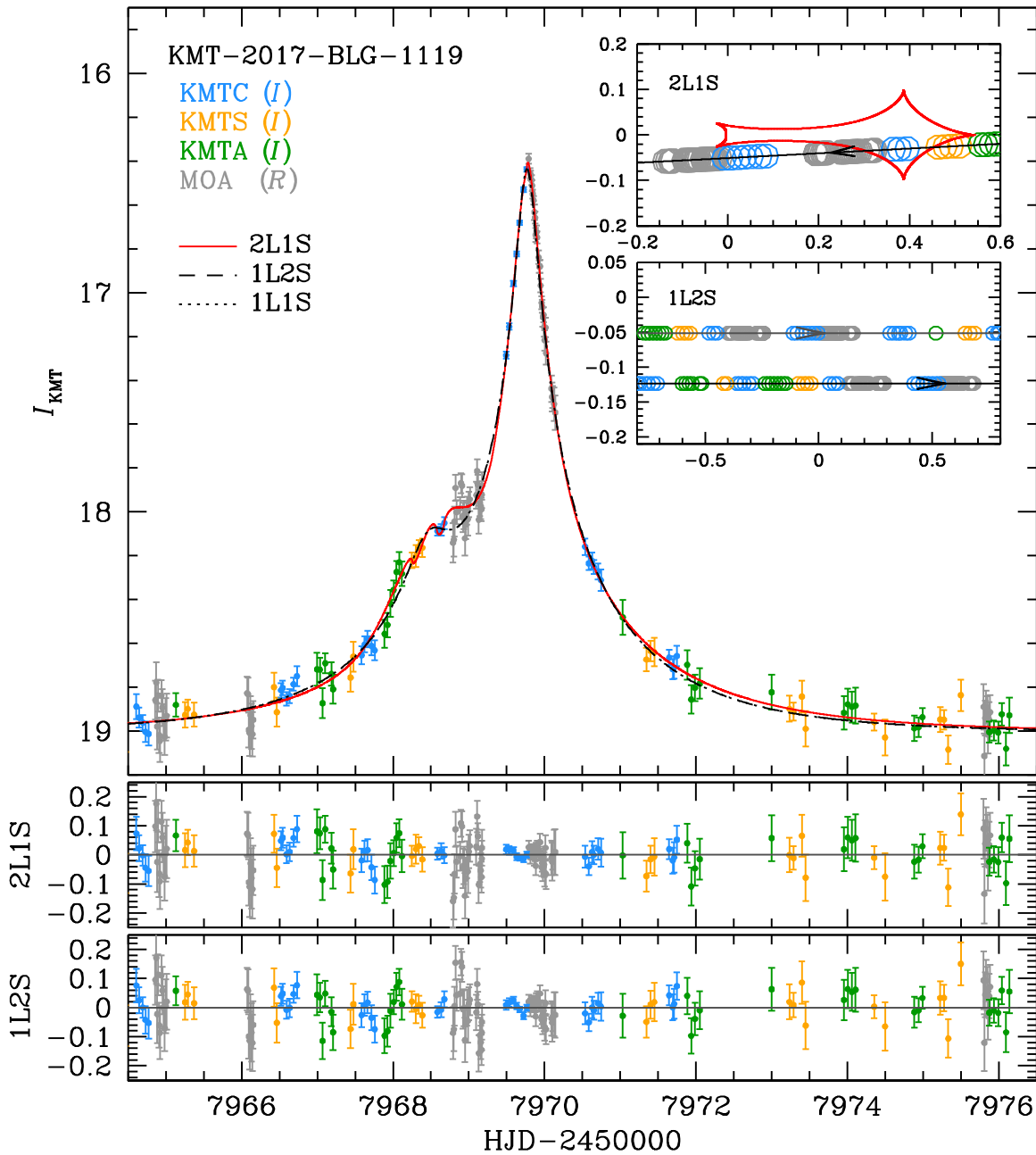
Figure 1. Degenerate models of KMT-2017-BLG-0962. The solid lines in red and blue indicate the 2L1S model light curves of the close and wide cases, respectively. The dashed line in black indicates the 1L2S model light curve. The dotted line indicates the 1L1S model light curve for this event. Left-side inner panels show a zoomed-in view of the anomaly part of the light curve with residuals. Right-side inner panels present geometries of 2L1S (top and middle panels for the close and wide cases) and 1L2S (bottom panel) models. Three bottom panels show residuals between each model and observations.

magnification of its 1L1S light curve. For the 1L2S model light curve, the final magnification is calculated by superposing magnifications of both sources weighted by the flux ratio of source stars. To describe the source trajectories, there are two parameterizations. The first parameterization (hereafter, A-type) describes the trajectory of each source, individually. In contrast, the second parameterization (hereafter, B-type) describes the barycenter motion of the binary-source system. Then, from the position of the barycenter, the position of each source is derived. In Appendix A, we provide detailed descriptions of these parameterizations and discuss the pros and cons of the two types. In this work, because the merits of the two types are different, we adopt the A-type for the basic 1L2S modeling (Sections 3.3 and 3.4). For testing the higher-order effects, we adopt the B-type (Section 3.4).

3.3. Degenerate Models

3.3.1. KMT-2017-BLG-0962

For KMT-2017-BLG-0962, we find that the observed light curve can be described using either 2L1S and 1L2S interpretations. In Figure 1, we present the observed data and model light curves of this event with geometries of the 2L1S and 1L2S interpretations. We also present residuals between the models and observations. In Table 1, we present the model parameters of best-fit models with χ^2 between the models and observations. The 2L1S model indicates that this event can be caused by a planetary lens system with a mass ratio of $q \sim 0.01$ between the lens components. However, there is a degeneracy between the close and wide solutions. At the same time, the 1L2S model implies that the event can also be caused by a

Figure 2. Degenerate models of KMT-2017-BLG-1119. The description is the same as for Figure 1.

binary-source system. The planetary model (2L1S models of the close and wide cases) and 1L2S model are completely degenerate. The χ^2 differences between 1L2S and 2L1S are only ~0.6 and ~0.3 for the close and wide cases, respectively. Thus, we cannot claim a certain planet discovery.

3.3.2. KMT-2017-BLG-1119

For KMT-2017-BLG-1119, we find that the observed light curve is also well described by both interpretations. In Figure 2, we present light curves of these degenerate models with their geometries and residuals. In Table 2, we present the parameters of these degenerate models. In contrast to the previous case, these models show slight variations. The best-fit model, 2L1S, shows a low-mass ratio ($q \sim 0.009$) with a very short Einstein timescale ($t_{\rm E} \sim 2.92$ days). This indicates that this event can be

caused by a low-mass planetary lens system. However, this event also can be well described by the 1L2S interpretation, which implies that the planet would not exist. Quantitatively, the χ^2 difference between 1L2S and 2L1S is $\Delta\chi^2 \sim 29.7$. This $\Delta\chi^2$ value is too marginal to claim the 2L1S/2L1S degeneracy is resolved considering the severe systematics of the observations (see residuals of Figure 2). The $\Delta\chi^2$ cannot be conclusive evidence to resolve the degeneracy (we discuss more details of the χ^2 difference in Section 4.1).

3.4. Higher-order Effects of the Interpretations

Even though both events have the 2L1S/1L2S degeneracy, it is possible that these events were caused by planetary lens systems. Thus, for the 2L1S interpretation, we check the possibility of measuring the annual microlens parallax (APRX;

Table 1
Best-fit Parameters of Degenerate Models of KMT-2017-BLG-0962

Parameter	2L1S (Close)	2L1S (Wide)	Parameter	1L2S
$\chi^2/N_{\rm data}$	1918.423/1918	1918.687/1918	$\chi^2/N_{\rm data}$	1919.026/1918
t_0 (HJD$'$)	$7872.514^{+0.009}_{-0.015}$	$7872.536^{+0.011}_{-0.011}$	$t_{0,S1}$	$7871.478^{+0.024}_{-0.029}$
u_0	$0.017^{+0.003}_{-0.002}$	$0.016^{+0.002}_{-0.001}$	$t_{0,S2}$	$7872.797^{+0.012}_{-0.024}$
t_E (days)	$33.380^{+2.966}_{-4.002}$	$35.513^{+3.026}_{-4.445}$	t_E	$34.435^{+3.215}_{-4.044}$
s	$0.529^{+0.012}_{-0.048}$	$1.964^{+0.210}_{-0.069}$	$u_{0,S1}$	$0.011^{+0.002}_{-0.002}$
q	$0.012^{+0.004}_{-0.002}$	$0.011^{+0.004}_{-0.002}$	$u_{0,S2}$	$0.015^{+0.002}_{-0.001}$
α	$2.723^{+0.006}_{-0.011}$	$2.725^{+0.006}_{-0.011}$	$q_{\rm flux}$	$4.099^{+0.844}_{-0.489}$
ρ_*	$\leqslant 0.010$	$\leqslant 0.009$	ρ_*	$\cdots$
$F_{\rm S,KMTC}$	$0.014^{+0.002}_{-0.001}$	$0.013^{+0.002}_{-0.001}$	$F_{\rm S,KMTC}$	$0.014^{+0.002}_{-0.001}$
$F_{\rm B,KMTC}$	$0.327^{+0.001}_{-0.002}$	$0.328^{+0.001}_{-0.002}$	$F_{\rm B,KMTC}$	$0.327^{+0.001}_{-0.002}$
$F_{\rm S,KMTS}$	$0.013^{+0.002}_{-0.001}$	$0.012^{+0.002}_{-0.001}$	$F_{\rm S,KMTC}$	$0.013^{+0.002}_{-0.001}$
$F_{\rm B,KMTS}$	$0.329^{+0.001}_{-0.002}$	$0.330^{+0.001}_{-0.002}$	$F_{\rm B,KMTC}$	$0.329^{+0.001}_{-0.002}$
$F_{\rm S,KMTA}$	$0.011^{+0.002}_{-0.001}$	$0.010^{+0.002}_{-0.001}$	$F_{\rm S,KMTC}$	$0.010^{+0.001}_{-0.001}$
$F_{\rm B,KMTA}$	$0.312^{+0.001}_{-0.002}$	$0.313^{+0.001}_{-0.002}$	$F_{\rm B,KMTC}$	$0.313^{+0.001}_{-0.001}$

Note. We present upper limits (3σ) of the ρ_* parameters for the 2L1S models. Because this event does not have caustic crossings, the ρ_* parameters are not accurately measured (see Figure 5). For the 1L2S models, the finite source effect is not considered for modeling.

Table 2
Best-fit Parameters of Degenerate Models of KMT-2017-BLG-1119

Parameter	2L1S	Parameter	1L2S
$\chi^2/N_{\rm data}$	1580.372/1579	$\chi^2/N_{\rm data}$	1610.081/1579
t_0 (HJD$'$)	$7969.731^{+0.002}_{-0.006}$	$t_{0,S1}$	$7968.468^{+0.044}_{-0.034}$
u_0	$0.051^{+0.003}_{-0.001}$	$t_{0,S2}$	$7969.769^{+0.003}_{-0.002}$
t_E (days)	$2.917^{+0.048}_{-0.110}$	t_E	$2.449^{+0.137}_{-0.189}$
s	$1.211^{+0.016}_{-0.001}$	$u_{0,S1}$	$-0.123^{+0.020}_{-0.032}$
q	$0.009^{+0.001}_{-0.001}$	$u_{0,S2}$	$-0.051^{+0.003}_{-0.005}$
α	$3.089^{+0.001}_{-0.006}$	$q_{\rm flux}$	$4.720^{+0.526}_{-0.679}$
ρ_*	$0.029^{+0.003}_{-0.001}$	ρ_*	$\cdots$
$F_{\rm S,KMTC}$	$0.185^{+0.007}_{-0.006}$	$F_{\rm S,KMTC}$	$0.248^{+0.030}_{-0.019}$
$F_{\rm B,KMTC}$	$0.210^{+0.006}_{-0.007}$	$F_{\rm B,KMTC}$	$0.147^{+0.017}_{-0.032}$
$F_{\rm S,KMTS}$	$0.157^{+0.003}_{-0.012}$	$F_{\rm S,KMTC}$	$0.206^{+0.033}_{-0.023}$
$F_{\rm B,KMTS}$	$0.256^{+0.012}_{-0.004}$	$F_{\rm B,KMTC}$	$0.208^{+0.021}_{-0.034}$
$F_{\rm S,KMTA}$	$0.145^{+0.007}_{-0.009}$	$F_{\rm S,KMTC}$	$0.212^{+0.031}_{-0.020}$
$F_{\rm B,KMTA}$	$0.251^{+0.009}_{-0.007}$	$F_{\rm B,KMTC}$	$0.184^{+0.018}_{-0.032}$
$F_{\rm S,MOA}$	$0.158^{+0.012}_{-0.002}$	$F_{\rm S,MOA}$	$0.221^{+0.024}_{-0.017}$
$F_{\rm B,MOA}$	$0.242^{+0.002}_{-0.012}$	$F_{\rm B,MOA}$	$0.179^{+0.014}_{-0.024}$

Note. For the 1L2S models, the finite source effect is not considered for modeling.

Gould 1992) because the microlens parallax is not only a key observable for directly determining the properties of the lens system but also a strong constraint for estimating the properties using the Bayesian analysis. However, we cannot find any meaningful improvements for both events to claim the detection of the APRX signals when we consider the APRX models by introducing the additional parameters of the microlens parallax.

For the 1L2S interpretation, the binary sources orbit each other and conserve their angular momentum. This source-orbital motion can affect the light curve. In addition, the source-orbital effect can be a clue to resolving the 2L1S/1L2S degeneracy. Thus, we test the effect of the source-orbital motion by adopting the B-type parameterization with two additional orbital parameters (see Appendix A for details about this parameterization). However, we cannot find any meaningful signals in the light curves of both events caused by the orbital motion of the sources

(for the details of non-detection of these higher-order effects, see Appendix B).

4. Resolving the Degeneracy

4.1. Detailed Analysis of the Light curve

We now consider whether the 2L1S/1L2S degeneracy can be resolved in either of the two events. There are several methods that may be employed to resolve this degeneracy, most of which were discussed by Gaudi (1998). The first method is the detailed analysis of the light curve to check for small differences between the two models.

For KMT-2017-BLG-0962, the χ^2 difference between the 2L1S and 1L2S models is insignificant, and Figure 1 shows that the three models are quite similar. In contrast to the Gaudi (1998) case, there are no caustic crossings. Only a smooth deviation exists from a 1L1S event. Thus, for this event, the differences in the light curve are not sufficient to resolve the degeneracy.

For KMT-2017-BLG-1119, the best 2L1S model is preferred by $\Delta\chi^2 \sim 30$ over the 1L2S model. However, even though the degeneracy is formally broken, the distinction is not as strong as it appears. In Figure 3, we present plots of the cumulative χ^2 of each model to investigate the origin of the χ^2 improvement. We find that the χ^2 improvement starts at HJD$' \sim 7969.0$, which is a part of the light curve covered by MOA and KMTC observations. The χ^2 improvement mostly comes from the MOA observations. Quantitatively, among the total χ^2 improvement, the MOA and KMTC data contribute $\Delta\chi^2 \sim 24$ and ~6, respectively. However, both data sets have systematics that persist even in the best model (see the bottom four panels of the zoomed-in view in Figure 3). This fact suggests that a significant portion of the improvement could just be from fitting systematics in the data. Thus, $\Delta\chi^2$ cannot be a conclusive clue to resolve the 2L1S/1L2S degeneracy. In addition, while this still indicates a preference for the 2L1S model, the physical parameters derived from the Bayesian analysis in Section 5.2.2 predict an extreme system in which the host itself is a massive planet. Thus, we should consider other means of testing the models to independently resolve the degeneracy.
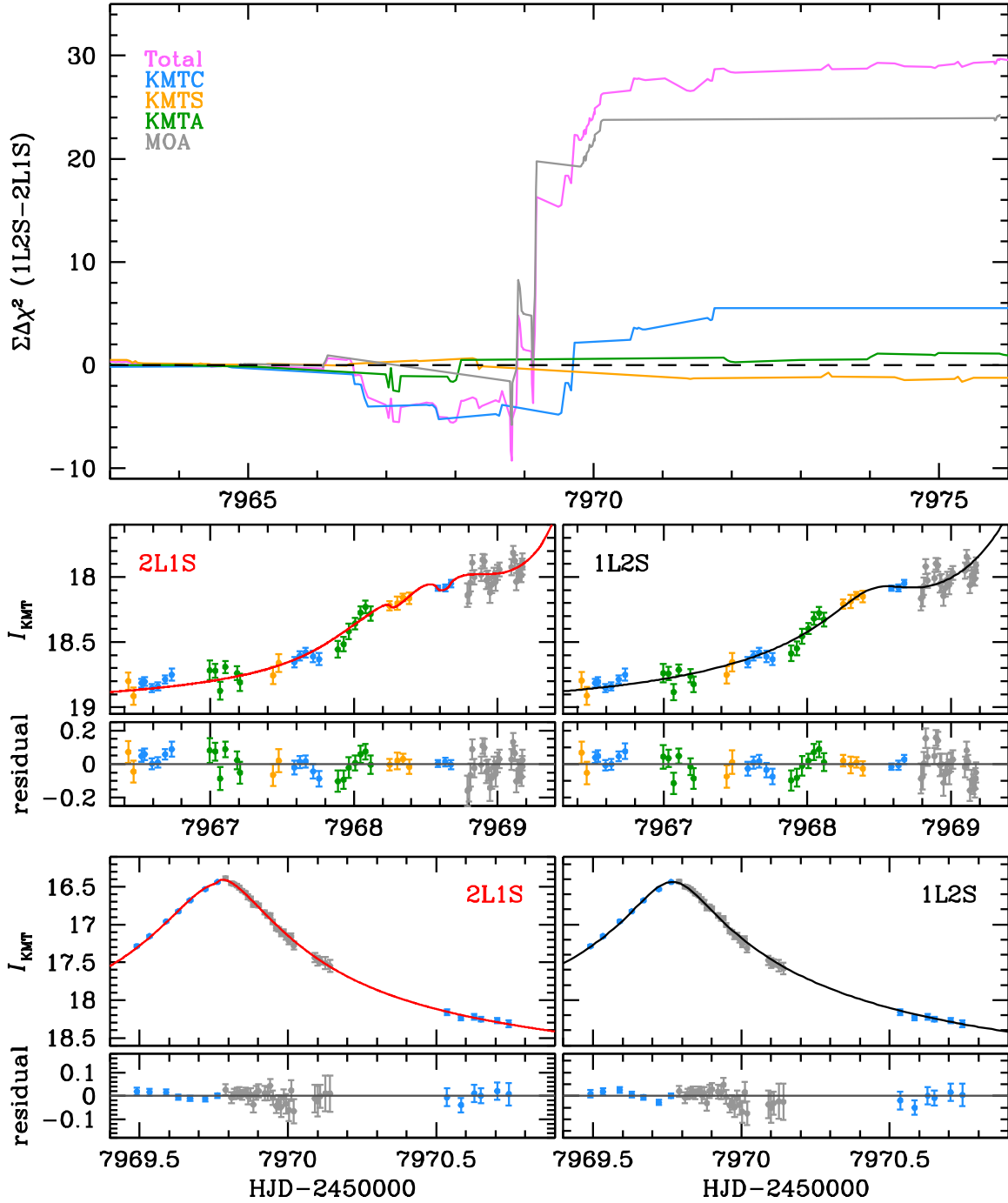
Figure 3. Cumulative χ^2 difference ($\Sigma\Delta\chi^2$) of degenerate models with zoomed-in views for anomaly part of KMT-2017-BLG-1119. The top panel shows the $\Sigma\Delta\chi^2$ of total and each data set. The bottom four panels present zoomed-in views of anomaly parts with residuals of each model case.

4.2. Color Information of the Source(s)

The second method is to use the source-color information. Because the magnification of the 1L2S model is a weighted mean using the flux ratio of the sources (see Appendix A), the final magnification is wavelength dependent. Thus, if the binary sources have different colors (and the event really is a 1L2S event), we can measure the color change or difference during the perturbation from multiband observations. However, unfortunately, the signal-to-noise ratio of V-band observations (the KMTNet regularly takes V-band images) for both events is too low to apply this method. Thus, we cannot resolve the degeneracy using this method.

4.3. Other Methods to Resolve the Degeneracy

Gaudi (1998) also proposed additional observations to resolve the degeneracy if the previous methods fail. One spectroscopic method requires taking spectra of the source both during and after the perturbations of the event. However, this method cannot be used after the events have ended. The other method requires photometrically and spectroscopically monitoring of the source after the event to search for other signals induced by the binary source such as radial velocity variations due to orbital motion or eclipses. Given the faintness of the source(s), spectroscopic monitoring would be challenging. And given the source separations ($0.04\,\theta_E$ and $0.5\,\theta_E$ for
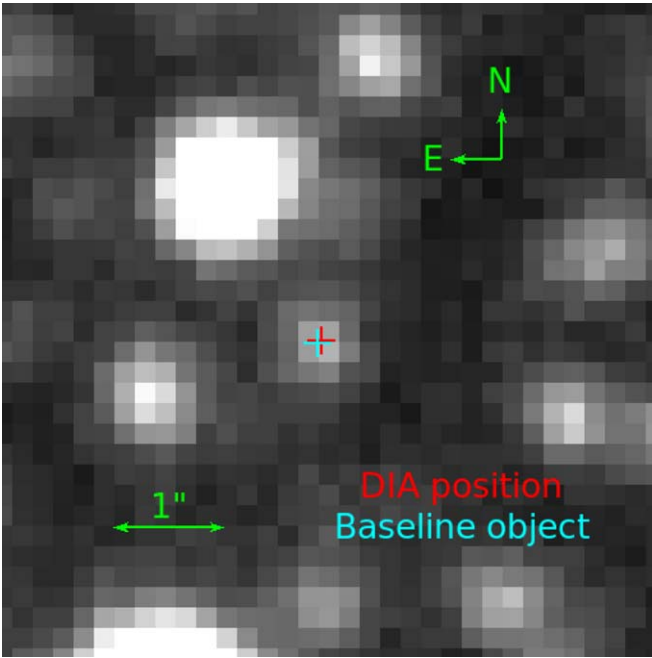
Figure 4. CFHT image with the astrometric offset ($0\overset{''}{.}037 \pm 0\overset{''}{.}009$) between the baseline object positions obtained from the CFHT image (cyan) and the KMTNet catalog (red) that is measured using the DIA. The green arrows indicate the north and east directions (top right) and a scale of $\sim 1''$ (bottom left).

KMT-2017-BLG-0962 and KMT-2017-BLG-1119, respectively), the probability of eclipses is extremely low. In addition, Calchi Novati et al. (2018) presented a new method to resolve the 2L1S/1L2S degeneracy using simultaneous ground- and space-based observations. However, unfortunately, space-based data do not exist for these events (see footnote 26).

4.4. Measurement of the Baseline Object

Because most possibilities, which are proposed by other studies, are not helpful to resolve the 2L1S/1L2S degeneracy of our cases, we consider another possibility to resolve the degeneracy using higher-resolution follow-up observations to directly measure the magnitude of the source(s) for these events. For KMT-2017-BLG-1119, we found different source fluxes ($F_{S,KMTC}$) for the 2L1S and 1L2S interpretations (see Table 2). If this event was caused by the planetary system, the magnitude of the source will be $I = 19.85 \pm 0.04$ and the lens is predicted to be dark. If this event was caused by binary sources, the integrated magnitude of the sources will be observed: $I = 19.54 \pm 0.11$. We note that these expected I magnitudes are calibrated to the OGLE-III magnitude system by crossmatching between KMTNet and OGLE-III catalogs ($I_{OGLE} = (0.0228 \pm 0.0125) + I_{KMTNet}$).

We check the expected brightness of the baseline object using observations taken from the Canada–France–Hawaii Telescope (CFHT) located at the Maunakea Observatories in 2018. In Figure 4, we present the CFHT image with the astrometric offset between the positions of the baseline object obtained from CFHT and KMTNet observations. The offset is $0\overset{''}{.}037 \pm 0\overset{''}{.}009$. From the CFHT image, we measure the brightness of the baseline object. We also see that the baseline object is close to coincident with the event and is isolated. Thus, it is highly likely that the light from the baseline object is composed of light from stars related to the event. Thus, the

CFHT measurement can be a constraint to check the degenerate solutions of this event. From the stacked deep CFHT image (seeing $\sim 0\overset{''}{.}7$), we can measure the brightness of the baseline object: $I_{base} = 19.62 \pm 0.05$ (we note that the CFHT instrumental magnitude is also calibrated to the OGLE-III magnitude system). The measurement of the baseline object is consistent with the expectation of the 1L2S interpretation considering its 1σ uncertainty. Therefore, this constraint supports the conclusion that this event might be caused by the 1L2S system. However, we cannot guarantee that the CFHT measurement completely excludes blend light from unrelated stars. Thus, the possibility of the 2L1S origin cannot be clearly ruled out, although it is disfavored.

The 2L1S solution predicts a lens-source relative proper motion of 4.7 ± 0.6 mas yr^{-1}. Thus, if a 30 m class telescope made observations a decade after the event and the relative proper motion of the source and lens were measured to be significantly different from 2L1S value, that would rule out that solution. On the other hand, if the proper motion were consistent with the 2L1S value, that would tend to support the planetary solution but would not be definitive. Note that such a measurement (as always) requires that the lens (or a companion to the lens) be luminous. However, the short timescale of this event favors low-mass lenses, which might fail this condition.

In contrast, for KMT-2017-BLG-0962, we obtained almost identical values of the F_S (see Table 1). Thus, for this event, the measurement of the baseline object using higher-resolution follow-up observations would not be helpful for resolving the degeneracy.

5. Properties of Planet Candidates

5.1. Bayesian Analyses

Because we cannot measure the microlens parallax, we estimate the properties of these planet candidates using the Bayesian analyses. We build a prior by generating artificial microlensing events (the total number of simulated events is 4×10^7). To generate these events, we adopt the Galactic models from various studies: initial and present-day mass functions of Chabrier (2003), velocity distributions of Han & Gould (1995), and matter density profiles of the Galactic bulge and disk of Han & Gould (2003). When these artificial microlensing events are generated, the line of sight to the actual event is considered. This prior contains various information about host properties according to the event rate. Based on the event rate, we calculate the posterior probability distributions of the lens properties, by applying constraints obtained from the actual event.

The constraints are built in the form of weight functions, which are obtained from the t_E and ρ_* distributions of the actual event. In Figures 5 and 6, we present the distributions of selected parameters (t_E, ρ_*, and q), the first two of which are used to build the weight functions and to determine the lens properties for KMT-2017-BLG-0962 and KMT-2017-BLG-1119, respectively. The distributions show a skewed Gaussian form, which we parameterize by

$$W(x) = \eta e^{-\frac{1}{2}\left(\frac{x-\mu}{\sigma}\right)^2} \left\{ 1 + \text{erf}\left[\frac{\alpha(x-\mu)}{\sqrt{2}\,\sigma}\right] \right\}, \quad (1)$$

where the function erf[z] indicates an error function defined as erf[z] = $(1/\sqrt{\pi}) \int_{-z}^{z} e^{-t^2} dt$. The variable x is t_E or ρ_*. The set of (η, μ, σ, and α) are fitting parameters. We use the MCMC
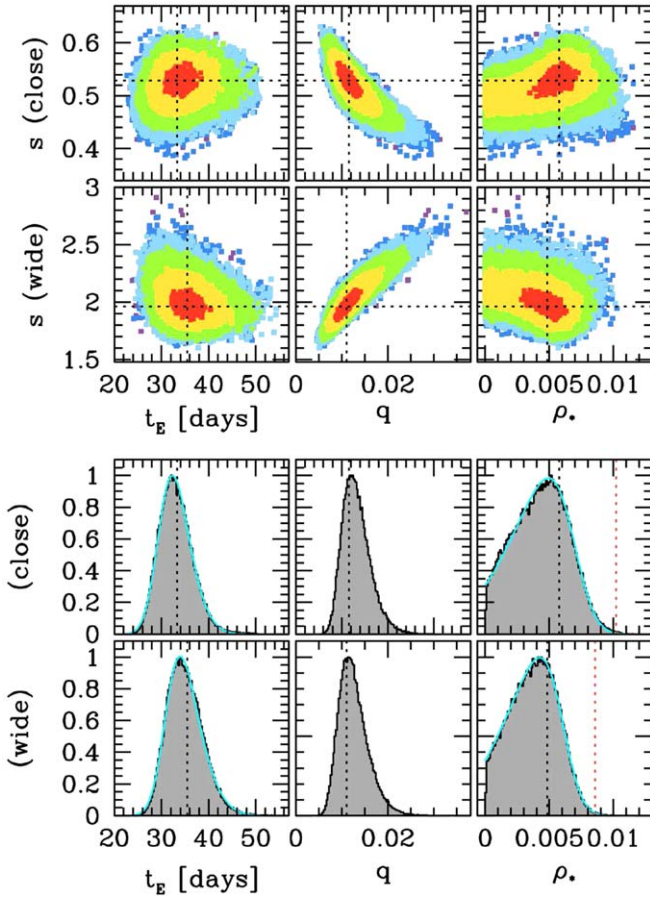
Figure 5. Distributions of t_E, q, and ρ_* parameters for KMT-2017-BLG-0962. The top six panels present 2D distributions for the close and wide cases of the 2L1S model obtained from the MCMC chains. Each color represents $\Delta\chi^2$ between realization on the chain and the best-fit model: 1^2 (red), 2^2 (yellow), 3^2 (green), 4^2 (sky blue), 5^2 (blue), and 6^2 (purple). The bottom six panels present 1D distributions of t_E, q, and ρ_* parameters for the close and wide cases. The cyan lines indicate weight functions constructed by the fitting of the skewed Gaussian function. The black dotted line indicates the parameter value of the best-fit model. The red dotted line in the ρ_* distributions represent the 3σ values.
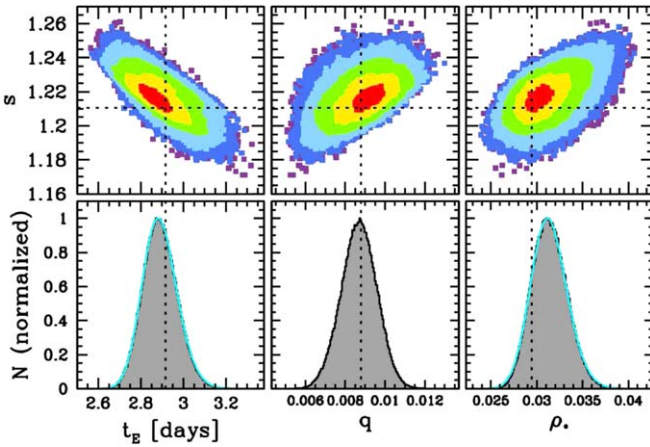
Figure 6. Distributions of t_E, q, and ρ_* parameters for KMT-2017-BLG-1119. The description is the same as for Figure 5.

algorithm to fit these parameters. The fitting results, i.e., t_E and ρ_* weight functions, $W(t_E)$ and $W(\rho_*)$, are presented in Figures 5 and 6 (cyan lines). In Table 3, we present the best-

Table 3
The Best-fit Parameters of Weight Functions

Event	KMT-2017-BLG-0962				KMT-2017-BLG-1119	
Model	Close		Wide		Resonant	
Parameter	$W(t_E)$	$W(\rho_*)$	$W(t_E)$	$W(\rho_*)$	$W(t_E)$	$W(\rho_*)$
η	0.706	0.593	0.672	0.597	0.766	0.780
μ	29.780	0.007	31.103	0.006	2.826	0.030
σ	4.745	0.004	5.452	0.004	0.105	0.003
α	1.683	-3.077	2.022	-3.164	1.285	1.201

fit parameter sets of $W(t_E)$ and $W(\rho_*)$ for both events. The final weight function is $W = W(t_E)W(\rho_*)$. By applying the final weight function to the event rate, we construct probability distributions of the host mass (M_L), the distance to the lens (D_L), the physical Einstein ring radius (r_E), and the lens-source relative proper motion (μ_{rel}). From these probability distributions, we can determine the properties of the planet candidate of each event.

5.2. Angular Source Radius

To apply the $W(\rho_*)$ to the event rate, the angular source radius (θ_*) is required to convert from θ_E (for the artificial lensing events) to ρ_* ($\rho_* = \theta_*/\theta_E$). However, unfortunately, we do not have reliable V-band data to estimate θ_*. Thus, we cannot adopt the conventional method (Yoo et al. 2004) using the ($V - I$) color of the source for measuring the θ_*. For each event, we estimate θ_* using different methods because the available observations are different.
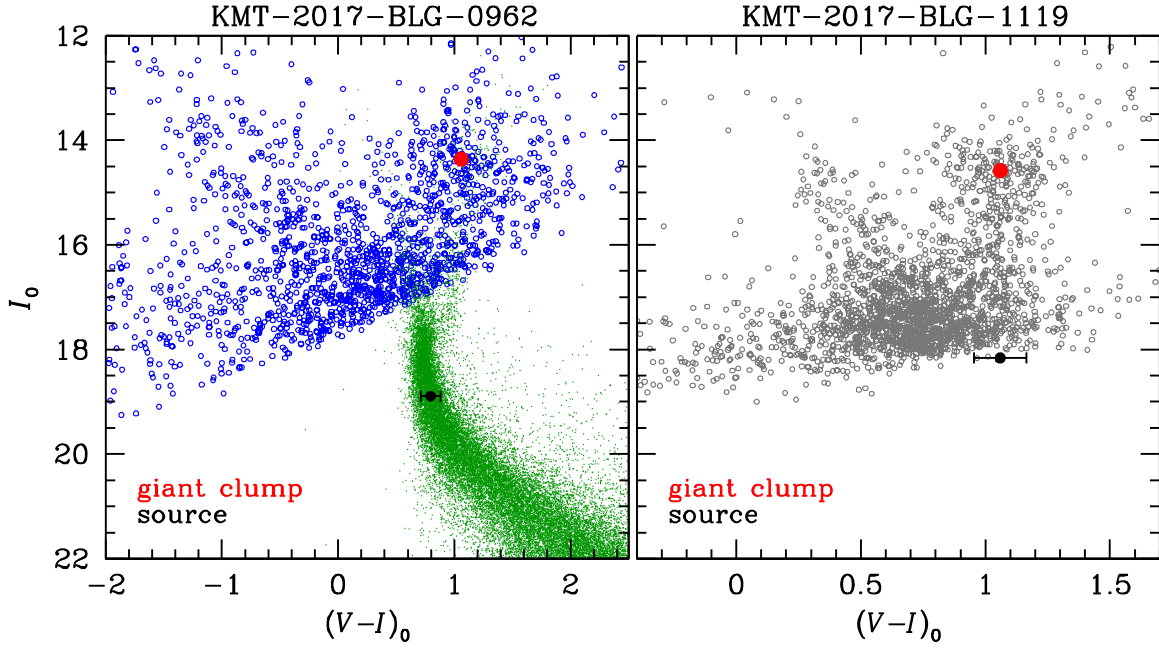
5.2.1. KMT-2017-BLG-0962

For this event, reliable observations to measure the source color do not exist. Thus, we adopt a statistical method (established in Bennett et al. 2008) to estimate the source color using *Hubble Space Telescope (HST)* observations of Baade's window (Holtzman et al. 1998).

The source magnitude offset from the red giant clump ($\Delta I_S = 4.531 \pm 0.110$) is determined from comparing the source flux ($F_{S,pyDIA}$) obtained from the pyDIA light curve to the red giant clump centroid measured from the color–magnitude diagram (CMD). Then, we extract *HST* stars that have similar magnitude offsets to those of the source of the event. Using this extracted *HST* star sample (and excluding 3σ outliers in $V - I$), we determine the median star color ($<(V - I)_{HST}>$) and the standard deviation of the color ($\sigma(V - I)_{HST}$). Then, we take this *HST* star color with uncertainty as a representative of the source color: $(V - I)_S = 1.357 \pm 0.083$. By adopting the clump color for the *HST* CMD from Bennett et al. (2008), we find that the offset of the source from the clump is $\Delta(V - I) = -0.263 \pm 0.083$. Then, using the intrinsic color (1.06; Bensby et al. 2011) and magnitude (14.362; Nataf et al. 2013) of the red giant clump along this line of sight, we derive: $(V - I, I)_{S,0} = (0.797 \pm 0.083, 18.893 \pm 0.110)$. Lastly, θ_* is estimated using the color/surface-brightness relation adopted from Kervella et al. (2004):

$$\theta_* = 0.58 \pm 0.06 \ \mu\text{as}. \tag{2}$$

In Figure 7, we present the combined CMDs of events where the centroids of the red giant clumps are aligned to the dereddened red giant clump magnitudes.

Figure 7. Combined CMD of KMT-2017-BLG-0962 (left) and KMT-2017-BLG-1119 (right), which are corrected for reddening. The green dots show the CMD of the Galactic bulge observed by the *HST* (Holtzman et al. 1998). The blue dots show the CMD of KMTNet constructed using pyDIA reductions. The gray dots show the KMTNet CMD dereddened and converted to the OGLE-III magnitude system. The red and black dots indicate the centroid of the red giant clump and the estimated source of each event, respectively.

5.2.2. KMT-2017-BLG-1119

For this event, MOA *R*-band observations exist. Thus, we can measure the $(R - I)$ color of the source from source fluxes of the model fits of MOA ($F_{S,MOA}$) and KMTNet ($F_{S,KMT,pyDIA}$) light curves: $(R - I_{KMT})_S = -24.684 \pm 0.021$. Then, we cross-match stars between the KMTNet and MOA CMDs with the OGLE-III catalog (Szymański et al. 2011) to derive a relation to convert $(R - I_{KMT})$ to $(V - I)_{OGLE-III}$. By combining the measured $(R - I)$ source color and conversion relation, we can determine the position of the source on the crossmatched CMD (in OGLE-III magnitude scales): $(V - I, I)_{S,OGLE-III} = (2.425 \pm 0.105, 19.891 \pm 0.042)$. Then, by adopting the method of Yoo et al. (2004) and the intrinsic color (1.06; Bensby et al. 2011) and magnitude (14.581; Nataf et al. 2013) of the red giant clump, we can measure the dereddened $(V - I)$ source color: $(V - I, I)_{S,0} = (1.060 \pm 0.105, 18.162 \pm 0.052)$. Then, we determine θ_* using the color/surface-brightness relation (Kervella et al. 2004):

$$\theta_* = 1.093 \pm 0.131 \ \mu\text{as}. \qquad (3)$$

In Figure 7, we present the dereddened KMTNet CMD with positions of the source and centroid of the red giant clump.

5.3. Bayesian Results

5.3.1. KMT-2017-BLG-0962

For KMT-2017-BLG-0962, we expect the θ_E constraint (combined with $W(\rho_*)$ and θ_*) to have only a weak effect on the Bayesian analysis because the constraint of $W(\rho_*)$ is weak for this event (see Figure 5). In addition, we have had to estimate θ_* by estimating the source $(V - I)$ using *HST* observations of Baade's window rather than making a direct measurement. Thus, we conduct Bayesian analyses with and without the θ_E constraint. In addition, the posterior distributions

are constructed using Galactic priors with and without stellar remnants as hosts of the lens system because we cannot rule out the possibility of stellar remnant hosts. Thus, for the degenerate 2L1S solutions (i.e., close and wide), we conduct four types of Bayesian analyses. In Figure 8, we present the results of the Bayesian analyses. In Table 4, we present median values of the distributions as representative of the lens system with 68% (1σ) confidence intervals. The Bayesian results both with and without the θ_E constraint are consistent considering the confidence intervals. The results indicate that this event can be produced by a planetary system consisting of a mid-M-dwarf host star and a super Jupiter-mass planet orbiting beyond the snow line.

5.3.2. KMT-2017-BLG-1119

For KMT-2017-BLG-1119, the 2L1S interpretation is disfavored considering the CFHT measurement of the baseline object. Although the 2L1S solution is disfavored, we report the Bayesian results for completeness. In Figure 9, we also present the probability distributions of the lens properties. Because the timescale of this event is particularly short, the distributions with and without stellar remnant hosts show identical results. Thus, we present one case. In Table 4, we also present median values of the distributions.

The Bayesian results suggest that the lens system of this event may be interesting. If the 2L1S solution is correct, the lens system is most likely to be a sub-Saturn-mass planet with a mass of $\sim 0.16 \ M_{Jupiter}$ ($\sim 0.53 \ M_{Saturn}$) orbiting a brown-dwarf host with a mass of $\sim 0.017 \ M_\odot$. Indeed, these kinds of planetary systems with faint/dark hosts ($M_h \lesssim 0.08 \ M_\odot$) were discovered by the microlensing method (e.g., Bennett et al. 2008; Han et al. 2013; Sumi et al. 2016; Shvartzvald et al. 2017; Jung et al. 2018a, 2018b; Miyazaki et al. 2018). Microlensing is one useful method to search these kinds of
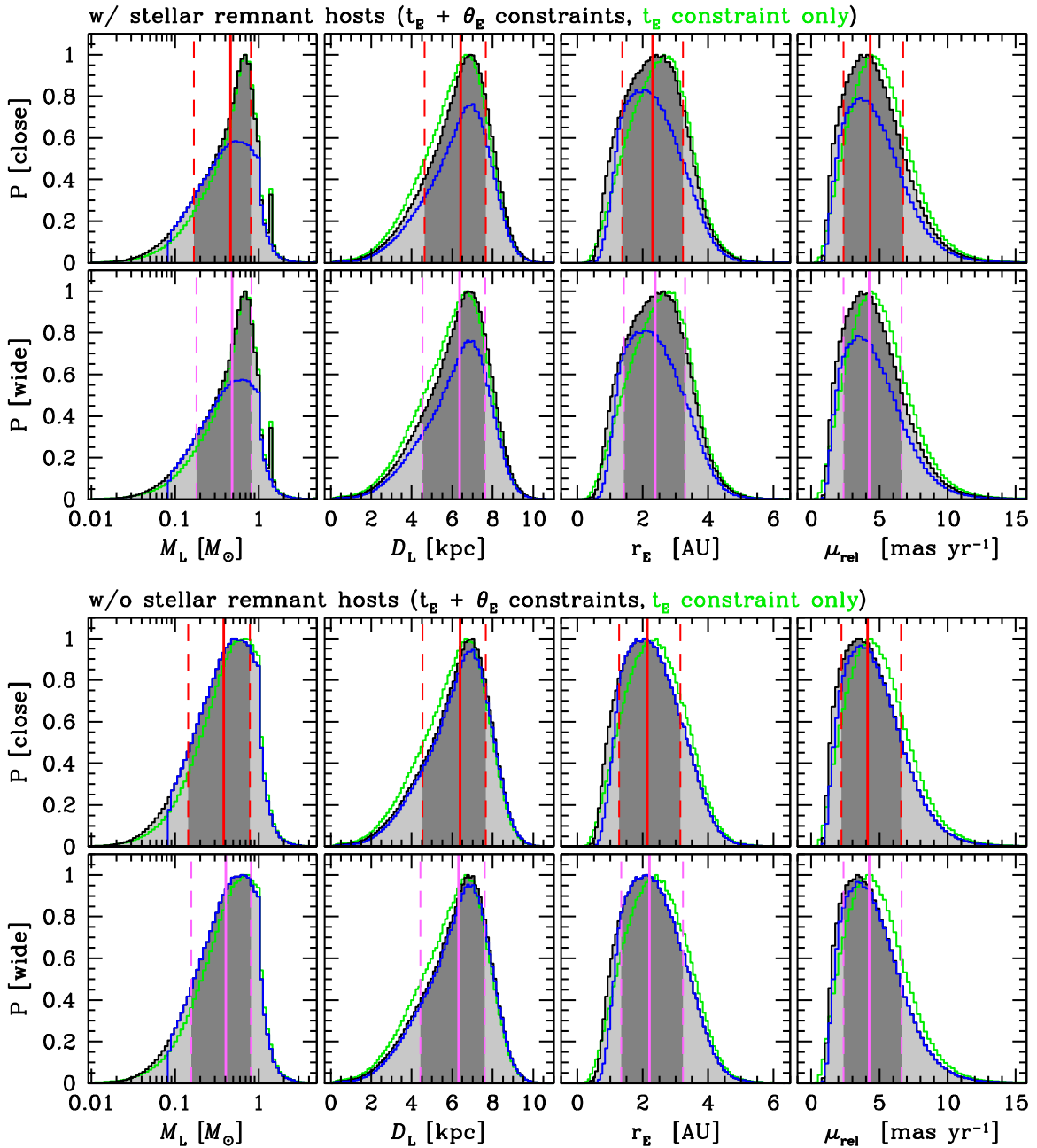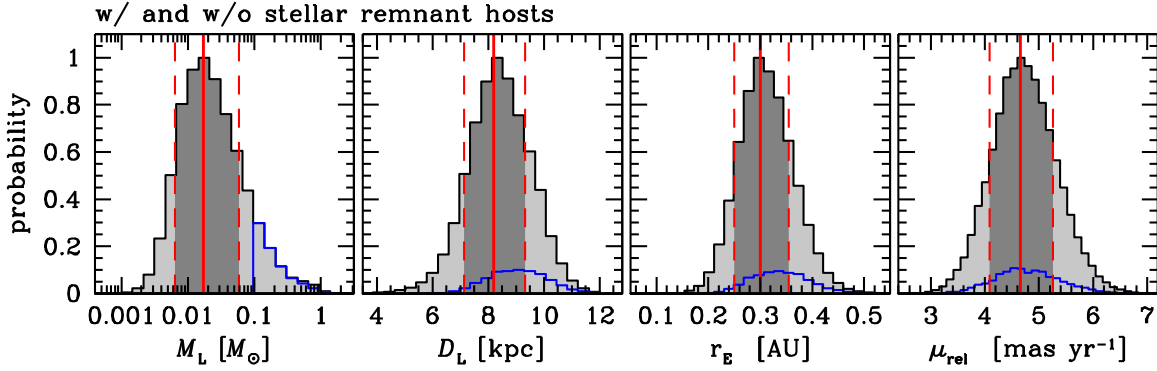
Figure 8. Probability distributions of the lens properties for KMT-2017-BLG-0962. The top six panels show the probability distributions of the host mass (M_L), the distance to the lens (D_L), the physical Einstein ring radius (r_E), and the lens-source relative proper motion (μ_{rel}) for the close and wide cases. These distributions are constructed from the Galactic prior with stellar remnant hosts. The bottom six panels show the probability distributions for the same lens properties, which are constructed from the Galactic prior without stellar remnant hosts. The solid and dashed vertical lines indicate the median value and 68% confidence interval (1σ uncertainty) of each property, respectively. The red and pink lines represent close and wide cases, respectively. The distributions in blue indicate the probability distributions including both the t_E and θ_E constraints considering only luminous hosts. The distributions in green indicate the probability distributions excluding the θ_E constraint.

systems because the method can discover planets regardless of the brightness of the hosts. However, we note that the 2L1S interpretation for this event is disfavored. Thus, it is unclear whether or not this event contains an example of such a planetary system.

6. Conclusion

We presented the analysis of two microlensing events with candidate planets. From the Bayesian analysis, we determine

the properties of the planet candidates. For KMT-2017-BLG-0962, the lens system may consist of a super Jupiter-mass planet and a mid-M-dwarf host. However, the severe 2L1S/1L2S degeneracy of this event, which is unresolvable, prevents claiming this planet discovery with certainty. For KMT-2017-BLG-1119, the 2L1S interpretation would indicate that the lens system consists of a sub-Saturn-mass planet and a brown-dwarf host. However, the CFHT imaging supports the 1L2S interpretation rather than this potential interesting planetary

Figure 9. Probability distributions of the lens properties for KMT-2017-BLG-1119. The description is the same as for Figure 8. In this case, the probability distributions with and without stellar remnant hosts are identical. Thus, we present only one case to avoid clutter.

Table 4
Properties of Planetary System Candidates

Event	KMT-2017-BLG-0962				KMT-2017-BLG-1119
Constraints	$t_E + \theta_E$		t_E Only		$t_E + \theta_E$
Model	Close	Wide	Close	Wide	Resonant
W/stellar remnants					
M_{host} ($M_\odot$)	$0.46^{+0.34}_{-0.29}$	$0.48^{+0.34}_{-0.30}$	$0.50^{+0.34}_{-0.31}$	$0.52^{+0.34}_{-0.31}$	$0.017^{+0.041}_{-0.011}$
M_{planet} (M_J)	$5.6^{+4.7}_{-3.7}$	$5.6^{+4.5}_{-3.6}$	$6.1^{+4.7}_{-3.8}$	$6.0^{+4.6}_{-3.7}$	$0.16^{+0.38}_{-0.10}$
D_L (kpc)	$6.4^{+1.3}_{-1.8}$	$6.4^{+1.3}_{-1.8}$	$6.2^{+1.3}_{-1.8}$	$6.2^{+1.3}_{-1.8}$	$8.2^{+1.1}_{-1.1}$
$a_\perp$ (au)	$1.2^{+0.5}_{-0.5}$	$4.7^{+1.9}_{-1.9}$	$1.3^{+0.5}_{-0.5}$	$5.0^{+1.8}_{-1.9}$	$0.36^{+0.07}_{-0.06}$
a_{snow} (au)	$1.2^{+0.9}_{-0.8}$	$1.3^{+0.9}_{-0.8}$	$1.4^{+0.9}_{-0.8}$	$1.4^{+0.9}_{-0.8}$	$0.05^{+0.11}_{-0.03}$
μ (mas yr^{-1})	$4.3^{+2.4}_{-1.9}$	$4.2^{+2.4}_{-1.9}$	$4.8^{+2.4}_{-2.0}$	$4.7^{+2.4}_{-2.0}$	$4.7^{+0.6}_{-0.6}$
W/o stellar remnants					
M_{host} ($M_\odot$)	$0.38^{+0.40}_{-0.24}$	$0.40^{+0.41}_{-0.25}$	$0.43^{+0.40}_{-0.26}$	$0.44^{+0.41}_{-0.27}$	
M_{planet} (M_J)	$4.7^{+5.2}_{-3.0}$	$4.7^{+5.1}_{-2.9}$	$5.2^{+5.3}_{-3.2}$	$5.1^{+5.1}_{-3.2}$	
D_L (kpc)	$6.4^{+1.3}_{-1.9}$	$6.3^{+1.3}_{-1.9}$	$6.2^{+1.3}_{-1.9}$	$6.1^{+1.4}_{-1.9}$	
$a_\perp$ (au)	$1.1^{+0.5}_{-0.5}$	$4.3^{+2.0}_{-1.7}$	$1.2^{+0.5}_{-0.5}$	$4.7^{+2.0}_{-2.0}$	
a_{snow} (au)	$1.0^{+1.1}_{-0.6}$	$1.1^{+1.1}_{-0.7}$	$1.2^{+1.1}_{-0.7}$	$1.2^{+1.1}_{-0.7}$	
μ (mas yr^{-1})	$4.1^{+2.5}_{-1.9}$	$4.1^{+2.4}_{-1.8}$	$4.6^{+2.4}_{-2.0}$	$4.5^{+2.4}_{-2.0}$	

Note. For KMT-2017-BLG-1119, the median values with and without stellar remnant hosts are identical. Thus, we present one case to avoid clutter.

system. The planetary solution could be tested with the possibility of conclusively ruling it out by a future measurement of the lens-source relative proper motion.

The 2L1S/1L2S degeneracies described in this work (and also the degeneracy in Jung et al. 2017b) are far different from the degeneracy for small, short-duration positive anomalies shown in Gaudi (1998). The anomalies are of a much longer duration and affect a significant fraction of the light curves, yet the degeneracy remains. In addition, the magnitude difference (ΔI) between the two sources is not very extreme ($\Delta I < 1.8$) in contrast to Gaudi (1998)'s case. These events are similar to the event recently analyzed in Dominik et al. (2019). These cases show that the 2L1S/1L2S degeneracy can exist for a wide range of planetary events and for much less extreme binary-source systems. Because binary stars are common and this degeneracy has proven not to be limited to a rare subset of

binaries, the 2L1S/1L2S degeneracy may be a bigger problem for the discovery of planets than previously thought.

Appendix A
Two Parameterizations of the 1L2S Interpretation

In Figure 10, we present conceptual geometries of the 1L2S interpretation for two types of parameterizations. The A-type parameterization (see the left panel of Figure 10) requires six parameters: $t_{0,S1}$, $t_{0,S2}$, $u_{0,S1}$, $u_{0,S2}$, t_E, and q_{flux} (Griest & Hu 1992). The first five parameters are directly related to the source trajectories: t_{0,S_1} and t_{0,S_2} are the time when each source most closely approaches the reference position (i.e., the position of the lens), u_{0,S_1} and u_{0,S_2} represent the closest separation between each source and the reference position at the time of t_{0,S_1} and t_{0,S_2}, respectively, and t_E is the Einstein timescale. We use one t_E parameter assuming that the lens-source relative speeds are same for both sources, i.e., a comoving binary-source system. The last parameter, $q_{flux} = F_{S_2}/F_{S_1}$ is the flux ratio of the sources. The role of q_{flux} is to weighting the two 1L1S light curves produced by the individual sources.

By adopting this parameterization, the position of each source as a function of time (t) is defined in Cartesian
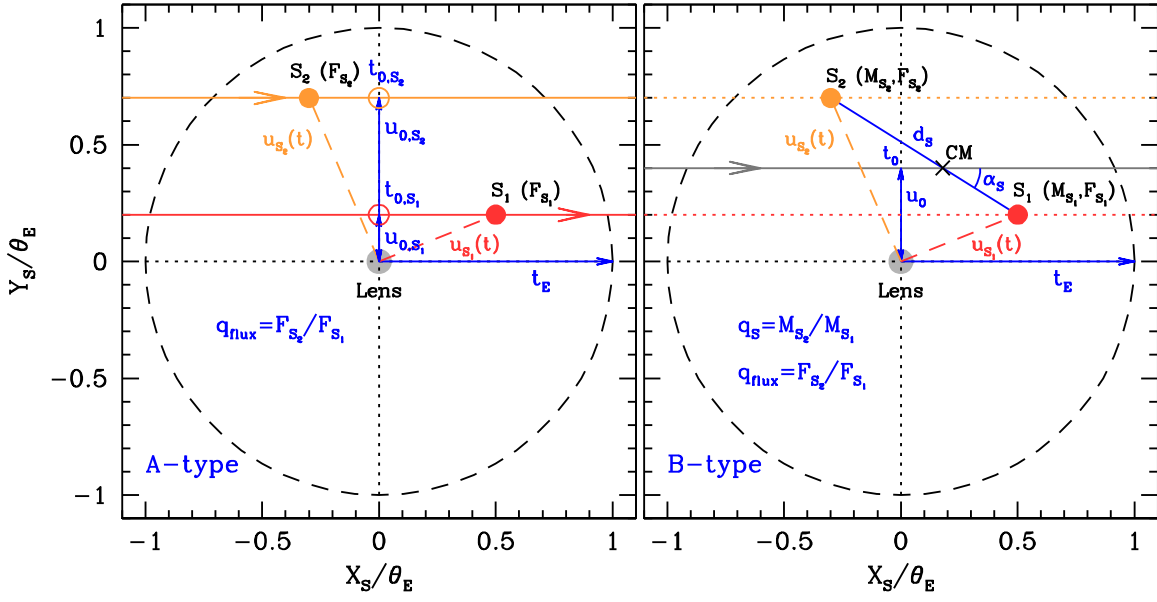
Figure 10. Conceptual geometries of the 1L2S interpretation. The left and right panels present the geometries of the A-type and B-type parameterizations, respectively. The blue text indicates parameters. The indices $i = 1$ and 2 indicate the first source (S_1) and second source (S_2), respectively. The F_{S_i} and M_{S_i} denote the flux and mass of each source. "CM" denotes the barycenter (i.e., the center of mass) of the binary-source system.

coordinates normalized by θ_E as

$$[X_{S_i}(t), Y_{S_i}(t)] = \left[\left(\frac{t - t_{0,S_i}}{t_E}\right), u_{0,S_i}\right]; \quad i = 1, 2. \quad (4)$$

According to the positions of the sources, the magnification of each source, $A_{S_i}(t)$, is defined as

$$A_{S_i}(t) = \frac{u_{S_i}^2(t) + 2}{u_{S_i}(t)\sqrt{u_{S_i}^2(t) + 4}};$$

$$u_{S_i}(t) = [X_{S_i}^2(t) + Y_{S_i}^2(t)]^{\frac{1}{2}}; \quad i = 1, 2. \quad (5)$$

These magnifications are superposed by weighting the ratio of source fluxes, $q_{flux} = F_{S_2}/F_{S_1}$. Then, the final magnification of the lensing light curve, $A(t)$, is calculated as

$$A(t) = \frac{A_{S_1}(t) + q_{flux} A_{S_2}(t)}{1 + q_{flux}}. \quad (6)$$

This model light curve in the magnification scale is converted to the flux scale of each data set for comparison to the observations using two additional parameters, F_S and F_B (similar to those of the 2L1S interpretation). These additional parameters are determined using the least-square fitting method.

The merit of this A-type parameterization is that it is possible to directly guess the initial values of most parameters (except q_{flux}) from the observed light curve. However, the A-type parameterization has a disadvantage in that it is difficult to apply higher-order effects, especially the orbital motion of the binary-source system.

Thus, we introduce an alternative parameterization, B-type (see the right panel of Figure 10), which considers the motion of the barycenter of the binary-source system (Jung et al. 2017b) rather than the motion of each source. To describe the barycenter motion, it requires three parameters (t_0, u_0, and t_E): t_0 is the time when the barycenter closely approaches to the

reference position, u_0 is the closest separation at the time of t_0, and t_E is the Einstein timescale. To derive the trajectory of each source from the barycenter trajectory, three additional parameters (d_S, q_S, and α_S) are required to describe the binary-source system: d_S is the projected separation between the sources, $q_S = M_{S_2}/M_{S_1}$ is a mass ratio of the source stars, and α_S is an angle between the axis of the binary-source and the barycenter trajectory. In addition, there is the last parameter (q_{flux}) that is identical to that of the A-type parameterization.

By adopting this parameterization, the source positions are defined as

$$\begin{bmatrix} X_{S_i}(t) \\ Y_{S_i}(t) \end{bmatrix} = \begin{bmatrix} X_{CM}(t) \pm r_{S_i} \cos \alpha_S \\ Y_{CM}(t) \mp r_{S_i} \sin \alpha_S \end{bmatrix}; \quad [X_{CM}(t), Y_{CM}(t)]$$

$$= \left[\left(\frac{t - t_0}{t_E}\right), u_0\right]; \quad i = 1, 2, \quad (7)$$

where the r_{S_1} and r_{S_2} are the separations between the barycenter and each source, which are defined as

$$r_{S_1} = d_S\left(\frac{q_S}{1 + q_S}\right); \quad r_{S_2} = d_S\left(\frac{1}{1 + q_S}\right). \quad (8)$$

Based on the positions of the source, the final model light curve is constructed in the same way as the previous parameterization (see Equations (5) and (6)).

This B-type parameterization has merit when higher-order effects are considered. In particular, the orbital motion of the binary source can be easily introduced because the binary-source positions are defined from the barycenter. To introduce the source-orbital motion, two additional parameters, dd_S/dt and $d\alpha_S/dt$, are required. These parameters are the variation rates of d_S and α_S to describe a partial orbit of the binary-source system. The variations are derived as

$$d_S' = d_S + \frac{dd_S}{dt}(t - t_{ref}); \quad \alpha_S' = \alpha_S + \frac{d\alpha_S}{dt}(t - t_{ref}), \quad (9)$$

where $t_{\rm ref}$ is a reference time for describing the orbital motion of sources (we set $t_{\rm ref} = t_0$ for the modeling in this work). Thus, the source trajectories are varied by the source-orbital motion, which are described by modifying Equations (7) and (8) as

$$\begin{bmatrix} X'_{S_i}(t) \\ Y'_{S_i}(t) \end{bmatrix} = \begin{bmatrix} X_{\rm CM}(t) \pm r'_{S_i} \cos \alpha'_{\rm S} \\ Y_{\rm CM}(t) \mp r'_{S_i} \sin \alpha'_{\rm S} \end{bmatrix}$$

$$\text{where } r'_{\rm S_1} = d'_{\rm S}\left(\frac{q_{\rm S}}{1 + q_{\rm S}}\right); \ \ r'_{\rm S_2} = d'_{\rm S}\left(\frac{1}{1 + q_{\rm S}}\right). \qquad (10)$$

However, the downside of this B-type parameterization is that it is particularly difficult to guess the initial parameters for describing the binary-source system (i.e., $d_{\rm S}$, $q_{\rm S}$, and $\alpha_{\rm S}$). Thus, usually, this parameterization is only adopted for testing higher-order effects.

Appendix B
Non-detections of Higher-order Effects

B.1. The Annual Microlens Parallax Effect of the 2L1S Interpretation

The APRX is caused by the orbital motion of Earth (Gould 1992). Thus, the Einstein timescale ($t_{\rm E}$) is a direct indicator for estimating the possibility of detecting the APRX signal. Empirically, to detect the APRX signal, the event should last more than $\sim$20 days. For KMT-2017-BLG-0962, $t_{\rm E}$ is about 33 days, which implies that there is a chance to detect the APRX signal in the light curve. Thus, we try to measure the APRX by introducing two additional parameters, $\pi_{{\rm E},N}$ and $\pi_{{\rm E},E}$, which indicate the north and east directions of the microlens parallax vector ($\pi_{\rm E}$), respectively. From the model considering the APRX, we find χ^2 improvements, 13.0 and 0.1, for the close and wide cases, respectively. However, these improvements originate in fits of systematics in the baseline, which are caused by an accidental caustic crossing and approach (see Figure 11). This fact implies that the APRX is not significantly constrained in these fits. Thus, we cannot extract any useful information from the APRX model for this event. For KMT-2017-BLG-1119, $t_{\rm E}$ is only 2.9 days, which implies that the APRX signal is unlikely to be present in the light curve. However, for consistency, we also test the APRX model for this event. From the model, as expected, the APRX signal is not detected.

B.2. The Source-orbital Effect of the 1L2S Interpretation

For the 1L2S interpretation, the binary sources always orbit each other to conserve their angular momentum. As a result, this source-orbital motion can affect the light curve if the microlensing event was caused by the 1L2S. It implies that once we may find the source-orbital effect on the lensing light curve, we can obtain a key clue to resolve the 2L1S/1L2S degeneracy. Therefore, we test the effect by introducing additional parameters of the simplified source-orbital motion (see Appendix A, B-type parameterization). The possibility of the detection of the source-orbital effect depends on the timescale of the event, which is similar to the APRX effect. As expected, for KMT-2017-BLG-1119, there is no χ^2 improvement considering the very short $t_{\rm E}$ of this event. In contrast, for KMT-2017-BLG-0962, we find a small χ^2 improvement ($\Delta\chi^2 \sim 8.7$) when the source-orbital effect is considered. We investigate this improvement using the cumulative χ^2 difference plot. See Figure 12. From the investigation, we find that the improvement mostly comes from the fitting of the "bump-like" feature in the baseline (HJD$' \sim 8000$). It is unclear whether this feature is real or due to some systematics in the baseline of the event. With $\Delta\chi^2 \sim 8.7$ for 2 additional degrees of freedom, the significance is too low to claim a detection.
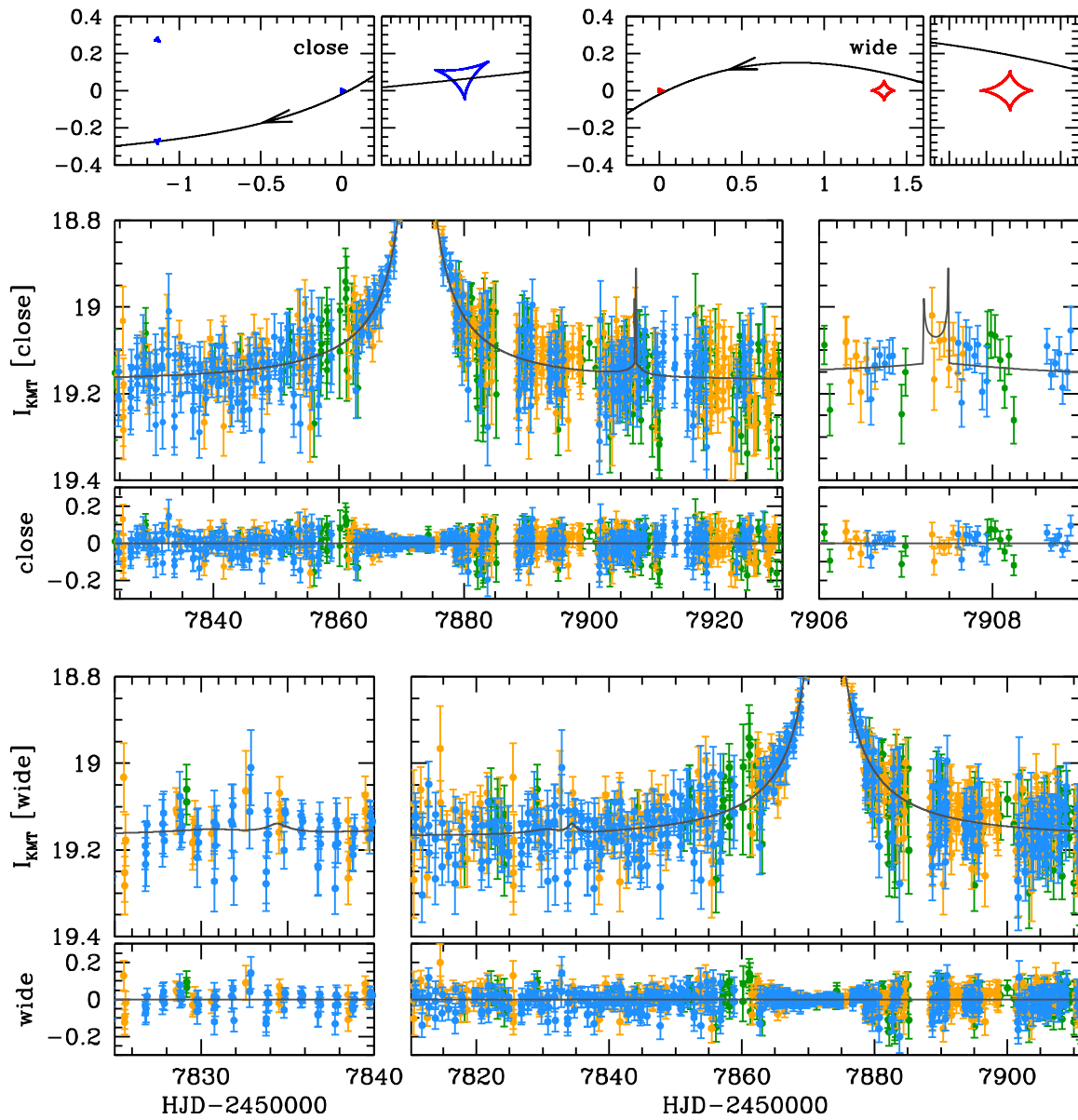
Figure 11. APRX models (2L1S) of KMT-2017-BLG-0962. The top panels show geometries of the APRX models for the close (left) and wide (right) cases with zoomed-in views of the caustic crossing and approach. The middle panels show the APRX model light curve (solid line) of the close case with a zoomed-in view where the part of the caustic crossing (left panels). The bottom panels show the APRX model light curve of the wide case. The zoomed-in view (right) shows the light-curve part where the caustic approach. The bottom panels of each light curve show residuals between models and observations. The color scheme of the observations is identical to Figure 1.
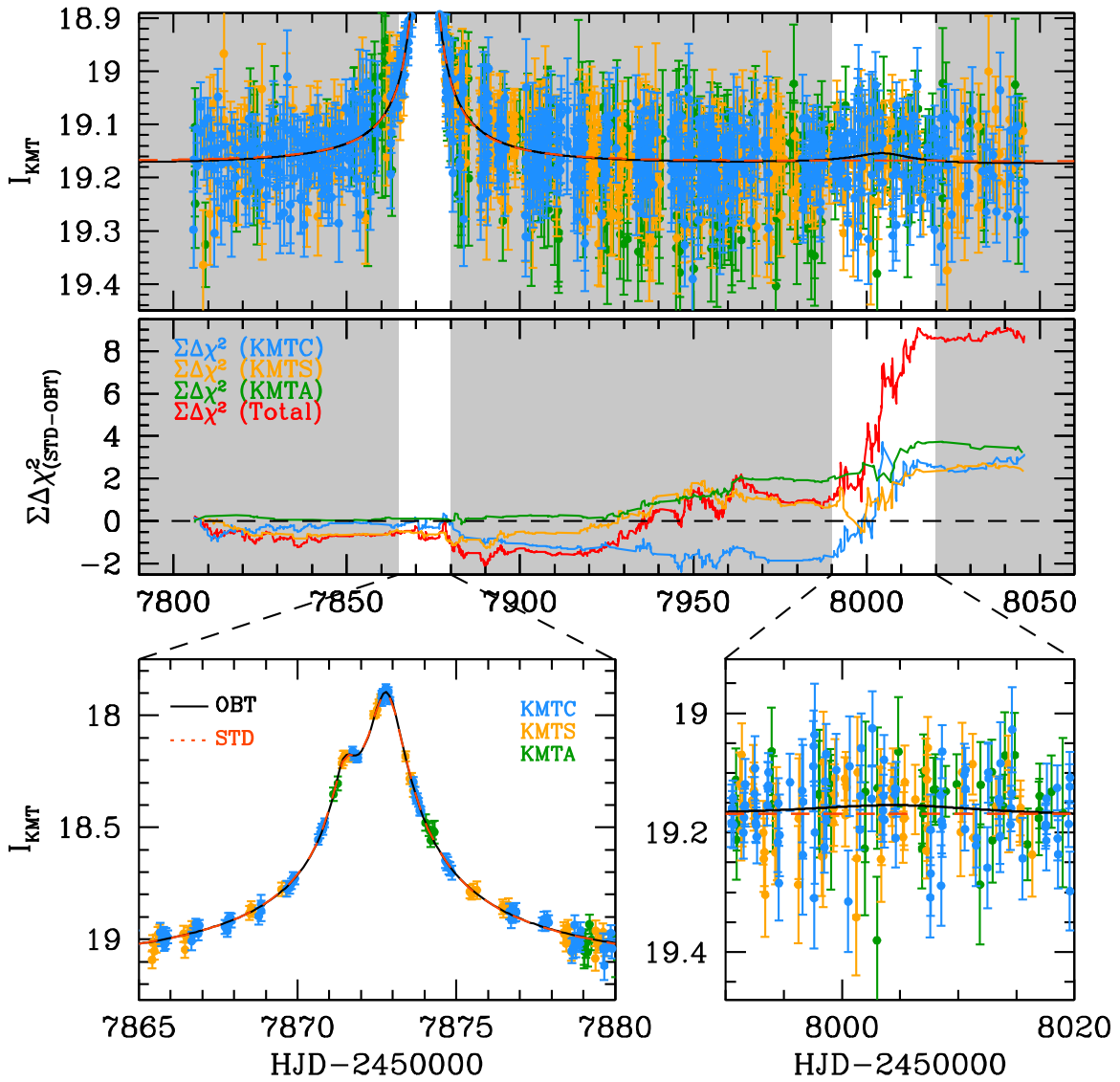
Figure 12. Cumulative χ^2 difference ($\Sigma\Delta\chi^2$) between static and source-orbital models (1L2S) of KMT-2017-BLG-0962. The top panel shows the whole baseline observations with static (scarlet dashed line) and source-orbital (solid black line) model light curves. The bottom panel presents the $\Sigma\Delta\chi^2$ of each data set. The boxes in white show light-curve zoomed-in views for the anomaly part (left) and the perturbation induced by the source-orbital motion effect (right).

ORCID iDs

I.-G. Shin ● https://orcid.org/0000-0002-4355-9838
J. C. Yee ● https://orcid.org/0000-0001-9481-7123
M. T. Penny ● https://orcid.org/0000-0001-7506-5640
M. D. Albrow ● https://orcid.org/0000-0003-3316-4012
S.-J. Chung ● https://orcid.org/0000-0001-6285-4528
C. Han ● https://orcid.org/0000-0002-2641-9964
K.-H. Hwang ● https://orcid.org/0000-0002-9241-4117
Y. K. Jung ● https://orcid.org/0000-0002-0314-6000
Y.-H. Ryu ● https://orcid.org/0000-0001-9823-2907
Y. Shvartzvald ● https://orcid.org/0000-0003-1525-5041
H.-W. Kim ● https://orcid.org/0000-0001-8263-1006
R. W. Pogge ● https://orcid.org/0000-0003-1435-3053
A. Fukui ● https://orcid.org/0000-0002-4909-5763
Y. Itow ● https://orcid.org/0000-0002-8198-1968
Iona Kondo ● https://orcid.org/0000-0002-3401-1029
S. Miyazaki ● https://orcid.org/0000-0001-9818-1513
C. Ranc ● https://orcid.org/0000-0003-2388-4534
N. J. Rattenbury ● https://orcid.org/0000-0001-5069-319X

Daisuke Suzuki ● https://orcid.org/0000-0002-5843-9433
W. Zang ● https://orcid.org/0000-0001-6000-3463

References

Beaulieu, J.-P., Bennett, D. P., Fouqué, P., et al. 2006, Natur, 439, 437
Bennett, D. P., Bond, I. A., Udalski, A., et al. 2008, ApJ, 684, 663
Bensby, T., Adén, D., Meléndez, J., et al. 2011, A&A, 533, A134
Bond, I. A., Abe, F., Dodd, R. J., et al. 2001, MNRAS, 327, 868
Calchi Novati, S., Skowron, J., Jung, Y. K., et al. 2018, AJ, 155, 261
Chabrier, G. 2003, PASP, 115, 763
Dominik, M. 1999, A&A, 349, 108
Dominik, M., Bachelet, E., Bozza, V., et al. 2019, MNRAS, 484, 5608
Dunkley, J., Bucher, M., Ferreira, P. G., et al. 2005, MNRAS, 356, 925
Gaudi, B. S. 1998, ApJ, 506, 533
Gould, A. 1992, ApJ, 392, 442
Griest, K., & Hu, W. 1992, ApJ, 397, 362
Griest, K., & Safizadeh, N. 1998, ApJ, 500, 37
Han, C., & Gould, A. 1995, ApJ, 447, 53
Han, C., & Gould, A. 2003, ApJ, 592, 172
Han, C., Jung, Y. K., Udalski, A., et al. 2013, ApJ, 778, 38
Holtzman, J. A., Watson, A. M., Baum, W. A., et al. 1998, AJ, 115, 1946

Hwang, K.-H., Choi, J.-Y., Bond, I. A., et al. 2013, ApJ, 778, 55
Hwang, K.-H., Udalski, A., Bond, I. A., et al. 2018, AJ, 155, 259
Jung, Y. K., Hwang, K.-H., Ryu, Y.-H., et al. 2018a, AJ, 156, 208
Jung, Y. K., Udalski, A., Bond, I. A., et al. 2017a, ApJ, 841, 75
Jung, Y. K., Udalski, A., Gould, A., et al. 2018b, AJ, 155, 219
Jung, Y. K., Udalski, A., Yee, J. C., et al. 2017b, AJ, 153, 129
Kervella, P., Thévenin, F., Di Folco, E., et al. 2004, A&A, 426, 297
Kim, D., Han, C., & Park, B.-G. 2009, JKAS, 42, 39
Kim, D.-J., Kim, H.-W., Hwang, K.-H., et al. 2018, AJ, 155, 76

Kim, S.-L., Lee, C.-U., Park, B.-G., et al. 2016, JKAS, 49, 37
Miyazaki, S., Sumi, T., Bennett, D. P., et al. 2018, AJ, 156, 136
Nataf, D. M., Gould, A., Fouqué, P., et al. 2013, ApJ, 769, 88
Shvartzvald, Y., Yee, J. C., Calchi Novati, S., et al. 2017, ApJL, 840, L3
Sumi, T., Abe, F., Bond, I. A., et al. 2003, ApJ, 591, 204
Sumi, T., Udalski, A., Bennett, D. P., et al. 2016, ApJ, 825, 112
Szymański, M. K., Udalski, A., Soszyński, I., et al. 2011, AcA, 61, 83
Yee, J. C., Gould, A., Beichman, C., et al. 2015, ApJ, 810, 155
Yoo, J., DePoy, D. L., Gal-Yam, A., et al. 2004, ApJ, 603, 139